A Comparative Study of Low-Level Jets in Different Climate Regions in China Using Multisite Doppler Wind Lidar Observations

Mengya Wang, Tianwen Wei, Simone Lolli, Francesc Rocadenbosch, *Senior Member, IEEE*, Andreu Salcedo-Bosch, Yu Du, Yuan Wang, Chenggang Wang, Lian Zong, Yefu Gu, Bingcheng Wan, Lian Su, Fangzhi Wei, and Haiyun Xia

***Abstract*—Low-level jets (LLJs) play a crucial role in modulating regional weather, air quality, and wind energy resources. In a topographically diverse country like China, the characteristics and driving mechanisms of LLJs are expected to vary significantly. However, a comprehensive understanding of these regional differences has been limited by the lack of coordinated, high-resolution observations. This study bridges this gap using a year-long observational experiment with Doppler wind lidars (DWLs) at three representative sites: Minfeng (MF) (temperate continental climate), Beijing (BJ) (temperate monsoon climate), and Hefei (HF) (subtropical monsoon climate). Our analysis reveals clear contrasts in LLJ regimes: boundary-layer jets (BLJs) dominate in MF and HF, while synoptic-system-related LLJs (SLLJs) prevail in BJ. LLJ-1 category is dominant at all three sites. A double-nose structure of BLJs is observed at 0.5 km in BJ and SLLJ peaks at 1.4 km in HF. Key properties such as jet core height, diurnal phase, and seasonal prevalence exhibit clear regional dependencies. The most frequent jet core heights are 0.7 km in MF, 0.4 km in HF, and 1.5 km in BJ, with peak seasonal activity occurring in May, July, and October, respectively. Jet core height increases with more stringent jet speed criteria at all sites. The time of the lowest LLJ occurrence frequency shows a longitudinal time lag, occurring at 14:00 local time in HF and BJ, and at 16:00 local time in MF, which aligns with the time of peak mixing layer height (MLH) at the corresponding site. The occurrence of nocturnal LLJs (NLLJs) is positively correlated with a deeper MLH, with occurrence frequencies exceeding daytime values during most of the night. The roles of inertial oscillations (IOs) and synoptic forcing in shaping LLJ characteristics are investigated. The most intense IOs occur near the jet core heights and are synchronized with frontal passage events at each site. Case studies of MF and HF suggest that frontal passages can amplify the IO signal, and the diurnal cycle of inertial motions associated with NLLJs is consistent with Blackadar's evening-transition hypothesis. Under strong synoptic forcing, such as in BJ, the IO signal becomes less pronounced. Analysis of synoptic forcing reveals distinct regional influences: in MF, NLLJs are favored by cold fronts, the Tarim easterly jets, and terrain-induced baroclinicity. In HF, they are influenced by the East Asian monsoon and frontal systems; and in BJ, the Northeast China Cold Vortex (NCCV) is the primary synoptic driver with significant influence from complex terrain. This study provides valuable observational insights into the regional variability of LLJs and their associated boundary-layer processes.**

***Index Terms*—Atmospheric boundary-layer dynamics, climate regions, inertial oscillations (IOs), low-level jets (LLJs), synoptic forcing.**

Received 19 November 2025; revised 23 January 2026; accepted 5 March 2026. Date of publication 11 March 2026; date of current version 31 March 2026. This work was supported in part by the Project of the National Key Laboratory of Climate System Prediction and Change Response under Grant CPRM-2025-NUIST-012, in part by the National Natural Science Foundation of China under Grant 42405136, and in part by the Universitat Politècnica de Catalunya (UPC)—Barcelona Tech Contributed through the Ministerio de Ciencia e Investigación (MCIN)/Agencia Estatal de Investigación (AEI)/10.13039/501100011033 and FEDER "Una manera de hacer Europa" under Project PID2024-155592OB-C21. *(Corresponding authors: Tianwen Wei; Haiyun Xia.)*

Mengya Wang, Tianwen Wei, Yuan Wang, Chenggang Wang, Bingcheng Wan, Fangzhi Wei, and Haiyun Xia are with the State Key Laboratory of Climate System Prediction and Risk Management (CPRM), School of Atmospheric Physics, Nanjing University of Information Science and Technology, Nanjing 210044, China (e-mail: twwei@nuist.edu.cn; hsia@ustc.edu.cn).

Simone Lolli is with CNR-IMAA, Tito Scalo, 85050 Potenza, Italy.

Francesc Rocadenbosch is with CommSensLab, Department of Signal Theory and Communications, Universitat Politècnica de Catalunya (UPC), 08034 Barcelona, Spain, and also with the Institut d'Estudis Espacials de Catalunya (Institute of Space Studies of Catalonia, IEEC), 08034 Barcelona, Spain.

Andreu Salcedo-Bosch is with CommSensLab, Department of Signal Theory and Communications, Universitat Politècnica de Catalunya (UPC), 08034 Barcelona, Spain.

Yu Du is with the School of Atmospheric Sciences, Southern Marine Science and Engineering Guangdong Laboratory, Sun Yat-sen University, Zhuhai 519082, China.

Lian Zong is with the Department of Civil and Environmental Engineering, The Hong Kong University of Science and Technology, Hong Kong, China.

Yefu Gu is with the Faculty of Applied Sciences, Macao Polytechnic University, Macau, China.

Lian Su is with the Institute of Optics and Electronics, Chinese Academy of Sciences, Chengdu 610207, China.

This article has supplementary downloadable material available at https://doi.org/10.1109/TGRS.2026.3672972, provided by the authors.

Digital Object Identifier 10.1109/TGRS.2026.3672972

I. Introduction

THE low-level jet (LLJ) refers to a mesoscale phenomenon characterized by a narrow band of enhanced wind speed and strong vertical wind shear occurring in the lower troposphere, typically below 2 km above ground level (AGL) [1], [2]. Although LLJs are vertically confined to a shallow layer, often only a few hundred meters, their horizontal extent can span several hundred kilometers [3]. These atmospheric features have been extensively investigated through observational campaigns [4], [5], [6] and numerical modeling efforts [7], [8], [9], [10]. These jets play a crucial role in modulating boundary-layer turbulence, facilitating vertical and horizontal transport of moisture and atmospheric pollutants, and contributing to regional momentum and energy exchange [11], [12], [13]. Given their significant impact on weather

and climate systems, a comprehensive understanding of LLJ characteristics and mechanisms across different geographic and climate regions is essential.

The occurrence and variation of LLJs are influenced by a complex interplay of mechanisms on various temporal and spatial scales [12], [14]. Among these mechanisms, the inertial oscillation (IO) theory is widely accepted, suggesting that IOs of ageostrophic components drive the diurnal cycle of LLJs [15], [16]. van de Wiel et al. [17] extended Blackadar's theory by incorporating frictional effects within the nocturnal boundary layer, but there are still some uncertainties remaining [18]. Other classical mechanisms to explain LLJ formation include terrain effects [19], [20], the upper-tropospheric jet [21], [22], and land-sea thermal contrasts [23], [24], [25]. Despite substantial progress, LLJ research in China is still insufficient compared to studies in the United States.

In recent years, studies on LLJs in China have multiplied, with a primary focus still placed on the relationship between LLJs and heavy rainfall events [26], [27], [28], [29], [30], [31]. Additionally, coastal LLJs have become another key research focus, particularly in relation to their role in marine-land interactions and mesoscale convection [32], [33], [34]. Several climatological studies have attempted to characterize LLJs in China. For example, Du et al. [35] first investigated the spatial and diurnal characteristics of LLJs in China using model data with a 9 km horizontal resolution from 2006 to 2011. Yan et al. [36] constructed a LLJ climatology over China and identified six high-frequency regions using radiosonde observations from 2011 to 2017. Ge et al. [37] examined nocturnal LLJs (NLLJs) and coincident dust events over the Taklimakan Desert based on ERA-Interim reanalysis and satellite observations from 2000 to 2013. Li et al. [38] investigated a LLJ climatology and its variability over the Bohai Sea and the Yellow Sea based on a 35-year hindcast dataset from 1979 to 2013. Miao et al. [39] conducted one-year wind profiler measurements in Beijing (BJ) (2015–2016) and Guangzhou (2013-2014), focusing on dominant synoptic types and their impacts on LLJ formation. Although these studies have contributed valuable regional insights, comparative analyses of LLJs across multiple geographic and climate regions within China are still lacking.

To address this gap, we selected three representative observation sites in different climate regions with different underlying surface conditions: BJ municipality in BJ-Tianjin-Hebei (BTH) region, Hefei (HF) in the Yangtze River Delta (YRD) region, and Minfeng (MF) County on the southern edge of the Taklimakan Desert. BJ has a typical warm temperate semihumid continental monsoon climate. Its complex terrain features such as the Taihang and Yanshan Mountains can influence the formation of LLJs by modulating the height and strength of the stable boundary layer through their effects on the inversion structure within the boundary layer [40]. HF is located in the transition zone between the subtropics and the warm temperate zone, characterized by a subtropical moist monsoon climate. In the region, LLJ development is primarily influenced by large-scale circulation patterns, synoptic processes, and the Asian monsoon system, which has practical implications for low-altitude economic activities [41]. MF county belongs to the warm temperate dry climate zone, the weather of which is influenced by the Tibet Plateau and the desert. This unique terrain configuration favors the formation of LLJ driven by cold downslope flow from the TP and strong surface thermal forcing from the desert, which together weaken the inversion layer and enhance jet development [42]. These three sites offer a comparative observational framework to investigate site-dependent differences in LLJ characteristics and driving mechanisms under distinct surface and environmental conditions in China.

Doppler wind lidar (DWL) enables continuous monitoring of vertical wind profiles with high temporal and spatial resolution [43], [44]. Building upon previous studies using Wind Profiler Radar in China [13], [45], DWL provides finer and more precise wind measurements, making it particularly well suited for the in-depth investigation of atmospheric boundary layer structure and dynamics. Most existing DWL-based LLJ studies have been conducted in U.S. Great Plains [46], [47]. In contrast, long-term lidar observations of LLJs across different surface types and climate regions in China remain scarce, particularly in arid and desert-edge regions. To fill this gap, this study performs a comparative analysis of LLJ characteristics over MF, HF, and BJ based on one-year Doppler lidar observations. To our knowledge, this is the first study to use year-round lidar measurements to compare the driving mechanisms of LLJs across different climate regions in China. The objectives of this study are threefold: 1) to characterize and contrast the LLJ properties across the three observational sites, focusing on jet core height distributions, directional patterns, diurnal, and seasonal variations; 2) to investigate the role of IOs in NLLJ formation, particularly the influence of frontal passages on enhancing IO amplitudes (AMPs) and the diurnal cycle of inertial motions; and 3) to explore the mechanisms of synoptic forcing and the relationship between mixing layer (ML) and NLLJs at the three sites.

II. Data and Methodology

A. Lidar Field Experiment and Data Collection

According to previous studies [36], LLJs occur most frequently in the Tarim Basin with a maximum occurrence rate of 31.0%. The YRD and BTH regions also exhibit high annual mean occurrence frequencies, both exceeding 18% during the period from 2011 to 2017. Therefore, we select three geographically and climatically distinct regions as the focus of this study: MF in the Tarim Basin, HF in the YRD region, and BJ in the BTH region.

We conduct one-year DWL observations at three sites: BJ (39.90°N, 116.34°E) from June 2022 to July 2023; HF (31.83°N, 117.25°E) from May 2021 to May 2022; and MF (37.06°N, 82.69°E) from January 2022 to December 2022. The geographical location of the three observational sites is shown in Fig. 1(a). Although the observational periods for the three sites do not fully overlap and could introduce seasonal or interannual variability, the overall LLJ patterns are expected to remain consistent due to the dominance of large-scale meteorological processes and boundary-layer dynamics that control LLJ formation.

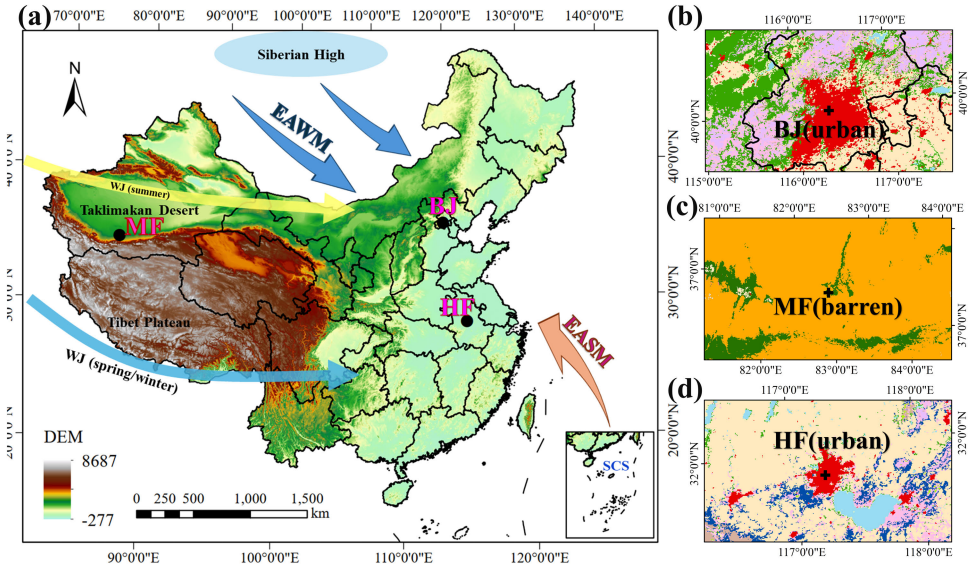

Fig. 1. (a) Locations of DWL observation sites (black dots) on the digital elevation model (DEM) of China. (b)–(d) MODIS land use and land cover type for the three sites. (b) BJ (39.98°N, 116.34°E), (c) HF (31.83°N, 117.25°E), and (d) MF (37.06°N, 82.69°E), respectively. In (b)–(d), red shading represents urban and built-up type and orange shading represents barren or sparsely vegetated type. The map is plotted using the Lambert Conformal Conic (LCC) projection with the WGS-84 datum. Abbreviations: SCS—South China Sea, EAWM—East Asia Winter Monsoon, EASM—East Asia Summer Monsoon, WJ—westerly jet, BJ—Beijing, MF—Minfeng, HF—Hefei.

Fig. 1(b)–(d) represents the land use and land cover types of the three sites, which are obtained from the Terra and Aqua combined Moderate Resolution Imaging Spectroradiometer (MODIS) Land Cover Dynamics (MCD12Q2) Version 6.1 data product with IGBP classification at 500 m spatial resolution in 2020 [48]. The underlying surface in MF is characterized by sandy land and sparse vegetation, and it is frequently affected by sand and dust storm events [49]. The HF site is located in metropolitan environment with dense building clusters dominating the surrounding area. BJ site is located within a densely urbanized area in Haidian, characterized by impervious surfaces, built-up infrastructure, and limited vegetation. MF is classified as barren land, while BJ and HF sites are characterized by impervious surfaces.

A compact coherent DWL system is deployed at all three sites to continuously monitor vertical profiles of aerosols, clouds, wind fields, and turbulence. The system operates at eye-safe wavelength of 1.5 μm and a repetition rate of 10 kHz to achieve a maximum detection range of up to 15 km. During the experiment period, the lidar operates in velocity azimuth display (VAD) scanning mode to enable high spatial-temporal resolution wind profile retrieval. For lidar measurements at each site, the availability of data is statistically estimated based on the number of valid days per month (Fig. S1). All wind profiles are processed using identical retrieval algorithms and consistent quality-control criteria at the three sites. Potential influences of site-dependent differences in aerosol loading and boundary-layer stability on data availability and measurement quality are acknowledged and discussed as an inherent limitation of multi-site Doppler lidar observations. The key operational parameters, system validation, and application performance can be seen in our previous work [50], [51], [52], [53]. We note that DWL provide direct turbulence measurements and reliable boundary-layer height estimates under daytime convective conditions. While their performance may deteriorate in the nocturnal stable boundary layer and is influenced by aerosol concentration, these factors are not the focus of this study, as it concentrates on atmospheric wind field detection.

ERA5 is the fifth-generation ECMWF reanalysis, providing global climate and weather data from January 1940 to present [Copernicus Climate Change Service (C3S), 2017]. It has been widely used to investigate the climatology of global LLJs [54], [55], [56]. In this study, ERA5 hourly data on pressure levels are obtained to compare and validate the LLJs characteristics retrieved from the lidar system. The Wyoming university radiosonde data are combined with lidar observations in the corresponding sites. These two datasets are openly accessible from the official websites.

B. Doppler Lidar Parameter Retrieval

The original radial velocity measurements obtained by the DWL have a temporal resolution of 1 s and a range gate resolution of 30 m. In the VAD algorithm, the horizontal wind speed, horizontal wind direction, and vertical wind speed are derived from the radial velocities across multiple azimuth angles using a filtered sinusoidal fitting technique, under the assumption of a horizontally homogeneous wind field [57]. Given the time required for a full VAD scan, the effective temporal resolution of the retrieved wind profiles is approximately 2 min. In this study, the wind direction of 0° corresponds to a flow originating from the north, increasing clockwise (CW). The vertical wind speed is defined as negative for the upward motion and positive for the downward motion.

TABLE I
CLASSIFICATION CRITERIA FOR THE FOUR TYPES OF LLJS BASED ON DOPPLER LIDAR MEASUREMENTS

LLJs category	V_{max} (m s^{-1})	ΔV (m s^{-1})
LLJ-1	$\geqslant 8$	$\geqslant 4$
LLJ-2	$\geqslant 12$	$\geqslant 6$
LLJ-3	$\geqslant 16$	$\geqslant 8$
LLJ-4	$\geqslant 20$	$\geqslant 10$

The turbulent kinetic energy dissipation rate (TKEDR) is commonly derived from vertical velocity variance, spectrum width, and structure function scaling [58]. In this study, TKEDR is estimated based on a turbulence statistical model that relates the structure function of the measured radial velocity to its theoretical form [59]. The ML height (MLH), which characterizes the vertical extent of turbulence-driven exchange within the planetary boundary layer [60], is subsequently identified. Specifically, the MLH is estimated as the altitude at which TKEDR decreases to the threshold of $10^{-4} m^2 \cdot s^{-3}$ from the surface [58], [61]. We note that the threshold is methodological rather than a universal definition. The accuracy of the retrieved MLH can be influenced by factors such as boundary-layer clouds, low carrier-to-noise ratios, and variations in atmospheric stability. Nevertheless, this threshold has been successfully applied in previous studies to determine the MLH over various surface types [53], [62].

C. Definition of LLJs Classification

LLJs are typically identified through the analysis of vertical wind profiles [1], [63]. According to previous climatological studies of LLJs in China [36], [39], the occurrence and intensity of LLJ at the three sites are determined based on the wind speed difference (ΔV) between the jet core wind speed (V_{max}) and the minimum wind speed (V_{min}) located above the jet core, within the lowest 3.5 km AGL. When multiple LLJ cores are present within a single wind profile, the lower LLJ is selected for analysis. Such multicore occurrences are rare during the observation period, observed on only 3 days at MF, none at HF, and 6 days at BJ. Each individual wind profile is evaluated to determine the occurrence of an LLJ event. To ensure statistical robustness, a 1-h moving window is applied to calculate the frequency of LLJ occurrence, filtering out spurious detections. Only time windows in which valid LLJ detections account for at least 60% of the total are retained for further analysis.

In this study, the classification criteria for LLJs are summarized in Table I. LLJ categories indicate the strength of the jet experienced, from the weakest jets in LLJ-1 to the strongest in LLJ-4. It is noted that the criteria for LLJ-1 differs from those of previous LLJ climatology studies based on wind profiler [25], [39] and radiosonde observations [36]. We adopt relatively smaller threshold values for both V_{max} and ΔV in order to capture weaker but dynamically significant boundary-layer LLJ events, which are frequently observed in Doppler lidar measurements. This adjustment accounts for the higher sensitivity and finer vertical resolution of the DWL, enabling the detection of subtle jet structures that may be overlooked by conventional observation platforms.

We compare the wind profiles retrieved from the DWL with those derived from ERA5 reanalysis and radiosonde observations during typical LLJ events. Considering that the ERA5 gridded data with a resolution of 0.25° may not accurately capture local wind characteristics at MF site due to the terrain influence from the Tibetan Plateau and the Taklimakan Desert, the ERA5-based comparison is limited to the HF and BJ sites. The height-time distributions of the horizontal wind speed, wind direction, and vertical wind speed are presented in Figs. S2 and S3. Overall, the spatial structures and magnitudes show good agreement between the two datasets. Comparisons between lidar and radiosonde observations are presented in Fig. S4 for the three sites. The results show generally good agreement, which confirms the reliability and consistency of the lidar-derived wind profiles in capturing key LLJ features.

D. Time–Frequency Analysis and Rotary Spectral Analysis

In contrast to linear, time-stationary analysis using classical Fourier transform (FT), the Hilbert–Huang transform (HHT) is a data-driven approach that is widely to process nonstationary and nonlinear signals [64], [65]. Whereas later Fourier-based approaches such as the short-time FT (STFT) and the wavelet transform use predetermined kernels (sinusoids or wavelets) and are limited by time–frequency uncertainty (STFT) or potential wavelet mismatch, the HHT derives its basis functions directly from the data. As a time–frequency analysis method, HHT consists of two major steps: empirical mode decomposition (EMD) and the Hilbert spectrum (HS). EMD adaptively decomposes a signal into a set of intrinsic oscillatory components, referred to as intrinsic mode functions (IMFs). An IMF must satisfy two essential conditions: 1) throughout the entire datasets, the number of extreme and zero crossings is either equal or nearly equal and 2) at any given time, the mean value of the envelopes defined by local maxima and minima is zero. In this study, the HHT method is employed to examine intermittent and nonstationary events, and to investigate IOs.

IOs arise from the Coriolis effect, which deflects moving air parcels to the right in the Northern Hemisphere, producing circularly polarized motions that rotate CW. In the Southern Hemisphere, these motions rotate counterclockwise (CCW). The characteristic timescale of this rotation, known as the inertial period, depends on latitude, given by $T = 2\pi/(2\Omega \sin\varphi)$, where Ω is the angular velocity of Earth and ϕ is the latitude. The evolving rotary spectral (ERS) analysis is capable of resolving the power of wind velocity at all frequency bands into CW and CCW components. The CW component is associated with a negative angular frequency, while the CCW component corresponds to a positive angular frequency. This approach has been proven effective in studies of directional or vector time-dependent observations, including ocean currents and wind data [66], [67], [68]. Therefore, both HHT and RES methods are used to investigate IOs in time-dependent wind data.

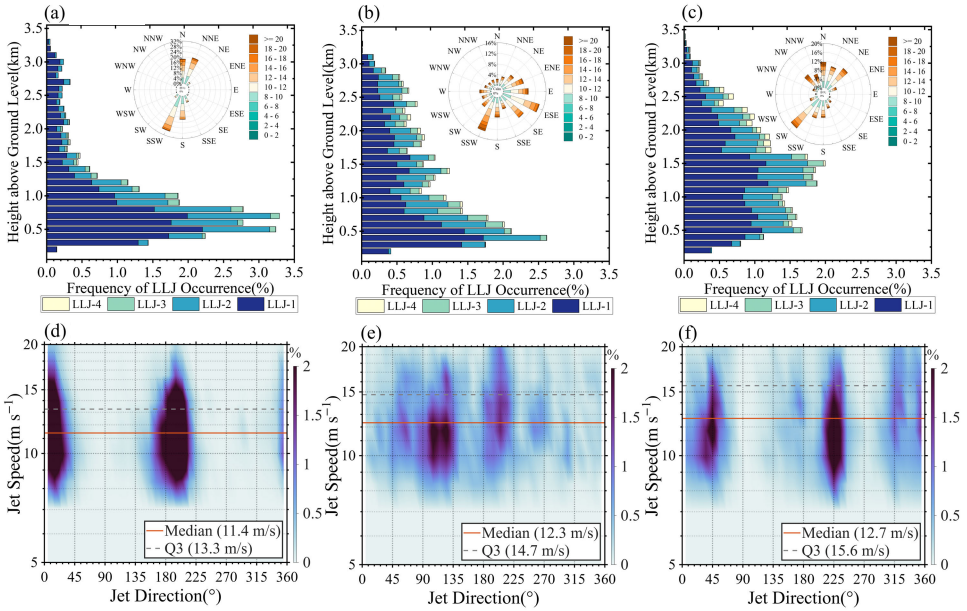

Fig. 2. Annual mean frequency (%) of occurrence for LLJ categories (LLJ-1 to LLJ-4) by height at the three sites (a) MF, (b) HF, and (c) BJ. Wind rose diagrams (a)–(c) summarize the horizontal wind speed and direction below 3.5 km at each site. Probability distributions (%) of LLJ speed by direction are shown for (d) MF, (e) HF, and (f) BJ. The *y*-axis represents jet speed (m · s^{-1}) on a logarithmic scale. The median and Q3 represent the second and third quartile, respectively.

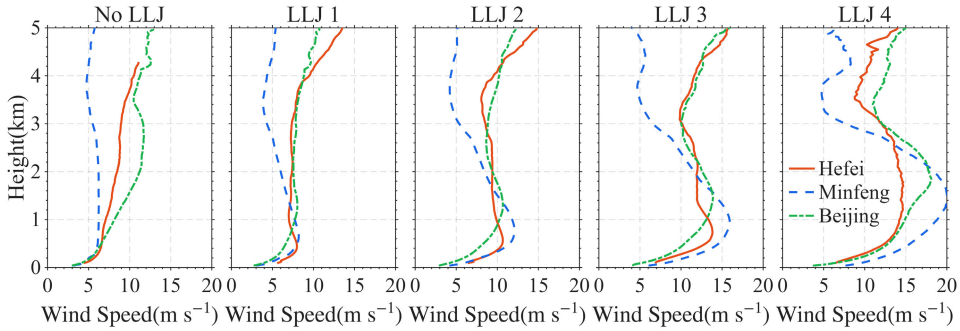

Fig. 3. Comparison of annual mean wind profiles on days without LLJ (labeled as "No LLJ") and with LLJ at MF (blue dashed line), HF (red solid line), and BJ (green dot dashed line). LLJ-1 to LLJ-4 represent the four LLJ categories.

III. Characteristics of LLJ at Different Sites

A. Overview of Wind Fields

During the one-year observation period, a total of 251 LLJ days are identified at MF, 185 days at HF, and 235 days at BJ. To better characterize the wind field associated with different LLJ categories, Fig. 2 presents the vertical distribution of annual mean frequency (%) for LLJ categories and the probability distributions (%) of jet speed by direction. Fig. 3 compares the vertical profiles of annual mean wind speed between LLJ and non-LLJ conditions. The frequency distributions in this section are used to characterize physically interpretable patterns in LLJ occurrence and structure across the three sites.

In this study, the frequency of LLJ occurrence (%) is determined at a given height defined as the ratio of LLJ profiles at that height to the total number of profiles. The annual LLJ occurrence frequency below 3 km is 32.7% at BJ, 29.5% at HF, and 27.9% at MF. As shown in Fig. 2(a)–(c), LLJ-1 is the most prevalent category, followed by LLJ-2, LLJ-3, and LLJ-4. Following the classification scheme with Du et al. [35], LLJs are divided into boundary-layer jets (BLJ)s, occurring below 1 km) and synoptic-system-related LLJs (SLLJs, occurring within 1–4 km). Consistent with this scheme, LLJs at MF and HF are primarily BLJs, whereas BJ shows a higher prevalence of synoptic-system-related LLJs (SLLJs, 21.5%). Furthermore, a double-nose structure in the frequency of BLJs occurrence is also identified at 0.5 km in BJ. Although less frequent than in BJ, SLLJs still represent a notable feature in HF, with a frequency peak at 1.4 km. The distinction of jet core heights at the three sites is corroborated by wind speed profiles in Fig. 3. The maximum wind speeds are observed below 1 km in MF and HF, but between 1 and 2 km in BJ. It is noteworthy to observe that the elevated jet core heights are associated with higher jet speed criteria at all sites.

For the vertical distribution [Fig. 2(a)–(c)], LLJs at MF and HF sites are largely confined below 1 km. MF displays a pronounced peak at 0.7 km (3.3%), while the occurrence frequency at 0.5 km (3.2%) is similarly notable. The most frequent layer of LLJs at HF is observed at 0.4 km (2.6%). These findings are consistent with the global climatological analysis of previous study [36]. While BLJs dominate in HF, SLLJs also frequently occur at 1.4 and 1.6 km (>1%). This feature is further supported by the wind profiles in Fig. 3, where LLJ wind speeds either remain steady or increase slightly with height. LLJ-2 to LLJ-4 categories are prominent above 1 km at HF, in contrast to the pattern at MF. In BJ, the total occurrence peaks at 1.5 km (2%), while LLJ-1 peaks at 1.2 km (1.2%). The frequency of SLLJs between 1 and 1.5 km (10.4%) is higher than that in other height ranges. This vertical pattern is consistent with previous study in the same region [39]. Moreover, LLJ-2 to LLJ-4 categories are more frequently observed above 1.7 km at BJ.

For the directional distribution, the predominant jet direction below 3.5 km varies between the sites in Fig. 2(d)–(f). The statistical results of mean, sigma, median, and the 3rd quartile (Q3) of jet speeds at the three sites are presented in Table SI. In MF, the probability distributions are strongly concentrated within two ranges (0°–45° and 180°–225°), with the median (11.4 m · s^{-}) and Q3 (13.3 m · s^{-1}) values being the lowest to those at the other sites. Fig. S5(a) further shows that LLJs occur most frequently in the 202.5°(~29%, SSW) and the 22.5° sectors (~22%, NNE). In contrast, HF exhibits a more evenly distributed jet direction pattern. The median and Q3 values are 12.3 and 14.7 m · s^{-1}. A primarily peak appears in the 90°–135° sector (>10 m · s^{-1}). At the category level in Fig. S5(b), relatively high frequencies are observed in the 112.5° (~15%, ESE) and the 202.5° sectors (~14%, SSW). In BJ, LLJs are most frequent within the 210°–240° sector, with the highest median (12.7 m · s^{-1}) and Q3 (15.6 m · s^{-1}) values. A secondary peak appears around the 45° sector, where most of jet speeds lie between 10 and 15 m · s^{-1}. Fig. S5(c) also highlights two preferred directions, which are 225° sector (~22%, SW) and the 45° sector (~15%, NE). Wind rose diagrams clearly illustrate the predominant northerly and north-northeasterly jets at MF, south-southwesterly jets at HF, and northeasterly jets at BJ below 3.5 km.

In Fig. 3, the wind profile in MF shows the weakest wind speeds during days without LLJ. By contrast, LLJ cases in MF show the strongest winds within the atmospheric boundary layer, suggesting the most frequent and intense BLJs. Yan et al. [36] reported that the main wind directions of the LLJ noses are NE and SW in MF, SW and NW in BJ, and SW and NE in the Huaihe River Basin region from 2011 to 2017. These findings are generally in agreement with the results of the present study.

B. Diurnal Variation of LLJ Occurrence

As a typical boundary-layer phenomenon, LLJs exhibit significant diurnal variability in their development and evolution. To explore this characteristic, the annual mean hourly occurrence frequency (%) of each LLJ category and the corresponding wind speed (m · s^{-1}) for LLJ days are presented in Figs. 4(a)–(c) and S5(d)–(f). The figures reveal a clear diurnal cycle in LLJ activity, accompanied by a contrasting trend of MLH [Fig. 4(d)]. The strongest diurnal signature is observed at MF, followed by HF. The most intense jet winds (>8 m · s^{-1}) occur between 0.4 and 0.8 km during 22:00–24:00 local standard time (LST) in MF [Fig. S5(d)], while it is observed between 0.3 and 0.8 km from 20:00 to 04:00 LST at HF [Fig. S5(e)]. In contrast, LLJ-related wind speeds at BJ [Fig. S5(f)] are more intense at higher altitudes (>1 km), reflecting a different vertical structure and potentially distinct forcing mechanisms.

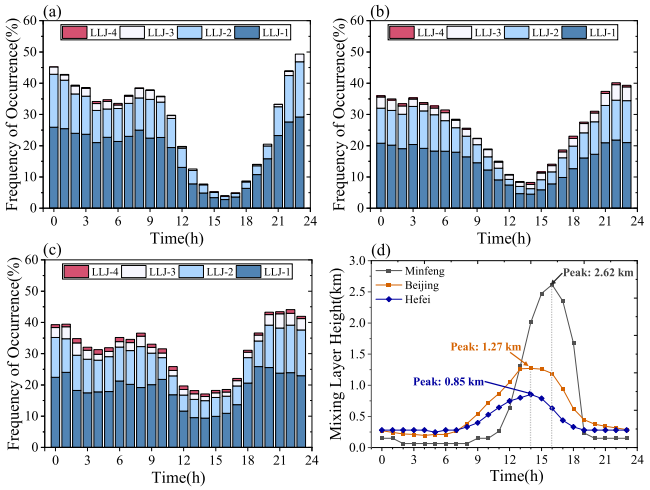

Fig. 4. Annual mean hourly occurrence frequency (%) of LLJ categories (LLJ-1 to LLJ-4) at (a) MF, (b) HF, (c) BJ, and (d) annual mean MLH at the three sites.

In general, LLJs intensify rapidly after sunset, peak around midnight, and weaken significantly after noon. Most events occur during nighttime and early morning, with LLJ-1 remains the dominant category throughout the day. The total frequency of occurrence exceeds 30% from 21:00 to 06:00 LST, forming a distinct "U"-shaped diurnal pattern across all sites. NLLJ generally account for more than 35% of the events, though the peak timing varies among locations. The maximum occurs at 22:00 LST (44.1%) in BJ and HF (22:00 LST, 40.1%), earlier than in MF (23:00 LST, 49.3%). In addition, LLJ-1 occurrence peaks at 19:00 LST (25.9%) in BJ, 22:00 LST (21.8%) in HF, and 23:00 LST (29.2%) in MF. A second small rise in LLJ frequency is observed from sunrise (06:00 LST), peaking at 08:00 LST in MF (38.5%) and BJ (36.5%). This morning rise is likely attributed to surface heating and changes in atmospheric stability, which enhances wind shear and intensify LLJs.

Afternoon LLJ activity is most prominent at BJ, where frequencies exceed 17% and stronger wind speeds (>10 m · s^{-1}) are observed above 2.2 km. LLJ-1 to LLJ-4 categories are consistently observed throughout the day at BJ, unlike at the other sites. The frequency of LLJ-1 occurrence peaks at 19:00 LST (25.9%) and 20:00 LST (25.6%), showing a reverse pattern compared to LLJ-2 through LLJ-4. The lowest jet speed category (LLJ-1) may be more sensitive to boundary layer changes, such as surface cooling

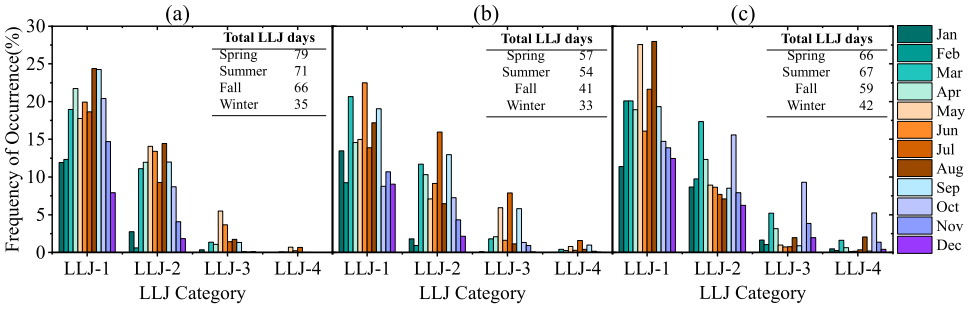

Fig. 5. Annual mean monthly frequency (%) of occurrence for LLJ categories (LLJ-1 to LLJ-4) at (a) MF, (b) HF, and (c) BJ. The total number of LLJ days for spring (March–May), summer (June–August), fall (September–November), and winter (December–February) at each site is provided in the embedded tables.

and atmospheric stabilization. Moreover, the terrain-induced gravity waves can modify the temperature structure in the atmosphere, affecting the temperature inversion layer above the jet zone and further influencing LLJ formation in BJ [40]. MF shows the lowest frequency at only 3.9%, with annual mean jet speeds below 3 m · s^{-1}. The time of the lowest LLJ occurrence frequency shows a longitudinal time lag, occurring at 14:00 LST in HF and BJ, and at 16:00 LST in MF. This pattern closely matches the corresponding diurnal variation in the peak height of MLH. It is due to the similar influence of solar heating and boundary layer dynamics, which causes both the LLJ occurrence and MLH peak height to follow the same diurnal cycle, with timing shifts influenced by local geographic and climatic conditions.

C. Seasonal Variation of LLJ Occurrence

Fig. 5 shows that LLJ-1 remains the dominant category throughout most of the months at all three sites, consistent with the vertical and diurnal occurrence patterns discussed earlier. However, noticeable monthly variations in frequencies of the LLJ category are evident at each site. LLJ days are more frequent in spring and summer while decreasing in fall and winter. The month of the most activity for all LLJ categories is May (38.0%) at MF, July (39.3%) at HF, and October (44.9%) at BJ.

LLJ-1 activity in MF increases from January to April and again from July to September, showing a bimodal pattern [Fig. 5(a)]. It is most frequent between March and October, with the overall occurrence frequency greater than 18% and peaking in August (24.4%). LLJ-2 follows a similar pattern, peaking in August (14.4%) and increasing from February to May and from July to August. LLJ-3 becomes more noticeable in May and June, though its maximum frequency remains relatively low (5.5%).

In Fig. 5(b), LLJ activity is more frequent in spring and summer in HF, and relatively rare in winter. LLJ-1 peaks in June (22.5%), followed by March (20.7%) and September (19.1%). In July, LLJ-2 (16.0%) surpasses LLJ-1 (13.8%), coinciding with a peak in LLJ-3 (7.9%). LLJ-3 shows high frequencies in May (5.9%) and September (5.8%). In BJ, LLJ-1 reaches a peak frequency in August (28.0%), followed by May (27.6), and maintains a frequency above 11% year-round [Fig. 5(c)]. Interestingly, LLJ-1 and LLJ-2 exhibit opposite trends from June to September. LLJ-2 peaks in March (17.3%) and exceeds LLJ-1 in October (15.6%), when LLJ-3 (9.3%) and LLJ-4 (5.2%) also reach their maxima.

To validate the analysis of LLJs, Fig. S6 shows the vertical, diurnal, and monthly variations in the frequency of occurrence for LLJ categories at the three sites based on the ERA5 reanalysis data. The general patterns are consistent with the results described above.

IV. Mechanisms Driving LLJ Formation

In this section, we first examine the role of IOs in the evolution of NLLJ. The period and spatiotemporal characteristics of IOs AMPs are analyzed and compared among the three sites. Second, the influence of the stable boundary layer on the development of NLLJ is investigated. Finally, we identify the dominant synoptic atmospheric circulation patterns associated with NLLJ events.

A. Influence of Frontal Passages on IOs

Under weak or in the absence of synoptic forcing and over terrain sufficiently open to allow the Coriolis force to influence the boundary layer dynamics, IOs emerge as the predominant driving mechanism of LLJ formation. As the stable nocturnal boundary layer (SBL) develops, surface friction no longer affects the horizontal flow in the residual layer. When the flow evolution is governed solely by the Coriolis force, undamped IOs around the geostrophic wind vector can drive the LLJ formation with the nose located in the residual layer [15]. Although IOs are ubiquitous in the atmospheric boundary layer, they are only with very small AMPs. As the SBL is subject to nonstationary phenomena, the HHT and ERS methods are utilized to identify both regular and intermittent events based on a one-year time series of Doppler lidar data.

Previous studies have noted that intermittent events (e.g., evening transition or frontal passage) can amplify the AMPs of IOs [69], [70]. To characterize these features, the ERS method is employed to examine the CW component of the rotary spectra and CW/CCW spectra ratio at varying heights using lidar observations at the three sites. A sliding window of 7–10 days with a 1-h overlap is adopted to balance spectral resolution and statistical robustness, while still capturing the intermittency of the IOs. In this study, the strongest IO windows are defined as those exhibiting the maximum CW

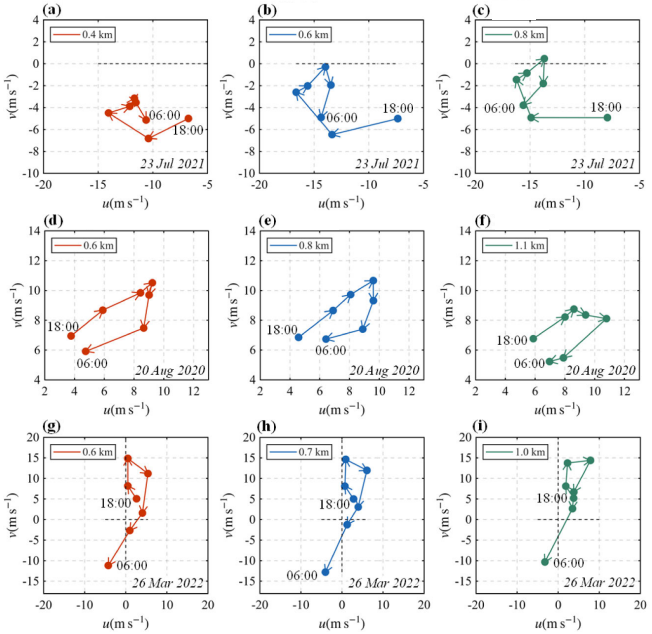

Fig. 6. Hodographs of wind velocity (18:00-06:00 LST) at the strongest IOs windows in (a)–(c) HF, (d)–(f) BJ, and (g)–(i) MF.

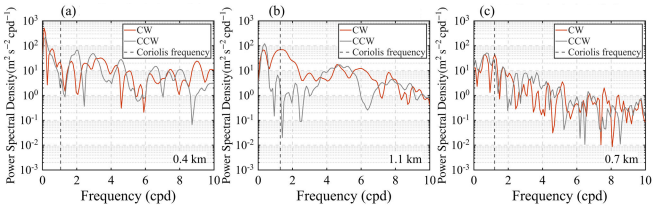

Fig. 7. Power spectra density ($m^2 \cdot s^{-2} \cdot cpd^{-1}$) at the window of maximum IOs calculated using the ERS method. CW and CCW denote CW and counterclockwise rotation, respectively. The inertial frequency corresponds to the local Coriolis frequency ($f = 2\Omega \sin\varphi$) and cpd refers to cycles per day. (a) ERS analysis in HF. (b) ERS analysis in BJ. (c) ERS analysis in MF.

spectra together with a CW/CCW spectra ratio greater than 2. Using a 7-day sliding window, the strongest IO windows (Fig. S7) are centered on July 23, 2021, at 0.4 km over HF, and August 20, 2020, at 1.1 km over BJ. Due to data availability, a 10-day sliding window is utilized for MF wind speed time series. The center days are March 25 and 26, 2022, at 0.7 km.

Furthermore, these windows are associated with frontal passage periods, and their heights correspond well with the most frequent jet core heights of LLJ occurrences [Fig. 2(a)–(c)]. Based on synoptic situation analysis, the BJ and MF cases are associated with cold fronts [Fig. S8(a) and (c)], while the HF case is influenced by a typical warm front linked to Typhoon In-fa [Fig. S8(b)]. To elucidate the evolution of the respective synoptic-scale conditions for each case, the vertical distributions of wind fields and air temperature from the ERA5 reanalysis datasets are analyzed (Fig. S9). The results show a clear temperature drop accompanied by strong northwest winds in the upper layers in BJ and MF. In contrast, the HF case is characterized by significant changes in wind field.

In Fig. 6, hodographs of wind velocity (18:00–06:00 LST) demonstrate clear CW-rotating motions for each NLLJ case at HF, BJ, and MF. In general, the strongest wind speed is observed at 22:00 LST in HF, 02:00 LST in BJ, and 00:00 LST in MF, respectively. The corresponding jet core height is 0.6 km in HF, 1.0 km in BJ, and 0.6 km in MF [Fig. 2(a)–(c)]. Consequently, the strongest IOs occur below the jet core height in HF but above the jet core height in MF and BJ. The CW motion in each case is further supported by the ageostrophic wind derived from ERA5 reanalysis data (Fig. S10).

Fig. 7 illustrates the power spectral density (PSD) due to IOs of the wind vector, which shows up as Coriolis-induced rotation of the wind vector and follows a CW pattern in the North Hemisphere. Differences between the PSD of the CW and CCW components are observed in each case, along with a comparison between the actual and theoretical inertial frequencies (Coriolis frequency, as described in Section II-D). The actual inertial frequency exhibits a small shift from the Coriolis frequency. Observed values are 1.03 cpd (23.3 h) in HF and 1.31 cpd (18.3 h) in BJ, compared to theoretical values of 1.06 cpd (22.6 h) and 1.29 cpd (18.6 h), respectively. In contrast, the observed inertial frequency of 1.21 cpd (19.8 h) in MF is identical to its Coriolis frequency. It is noted that the inertial frequency can be converted to hours using the equation $T = 24/f_{cpd}$, where T is the period in hours and f_{cpd} is the frequency in cpd.

Building on ERS analysis, we further employ the HHT technique to gain a comprehensive understanding of the instantaneous amplitude of IOs, following previous studies [25], [69], [71]. The lidar dataset is processed at its native vertical resolution of 26 m and the EMD technique is applied to the time series at each height level. The IMF sifting and identification process yields between four and six IMFs at each vertical level. At most levels below 2 km, an IMF with a period of approximately equal to the Coriolis frequency in hours is identified at the three sites. The U and V wind components at 0.4 km [Fig. 8(a) and (b)] are used as a representative example for the HF case. At this level, IMF6, which denotes the sixth mode sifted out by the spectral decomposition algorithm, exhibits a period of ~23 h on 23 July [Fig. 8(c) and (d)], which corresponds well to the IO period in HF identified by the ERS analysis. Furthermore, the HHT analysis of the composite wind speed [Fig. S11(a)] shows a consistent IO period [Fig. S11(b)], confirming the IOs mechanism of the NLLJ in the atmospheric boundary layer over HF.

After identifying the IMFs, the Hilbert transform is applied to each component to derive their instantaneous frequencies and AMPs. Fig. 8(d) and (e) presents the instantaneous amplitude of IM6 along with its mean value (A) and one standard deviation ($A \pm \sigma$). The instantaneous amplitude of the U wind component increases on 22 July and peaks on 23 July [Figs. 8(e) and (f) and S11(c)]. The period from 18 to 23 July has been identified as having IOs during NLLJ events based on ERS analysis and wind velocity hodographs. The periphery of Typhoon In-fa begins to influence HF on 23 July, bringing with it strengthened easterly winds in the upper atmospheric boundary layer [Fig. S9(b)]. Consequently,

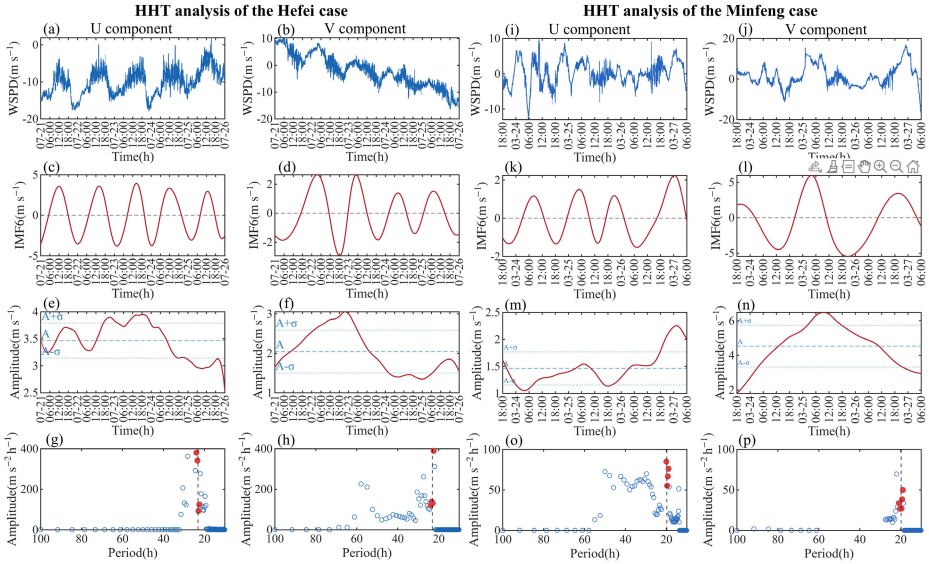

Fig. 8. HHT analysis. (a) and (b) Raw signals of the U and V wind speed components at 400 m, (c) and (d) corresponding IMFs6), (e) and (f) instantaneous AMPs, and (g) and (h) marginal HS amplitude of IMF6 in HF. The red dots are located in the actual IO frequency bands. (i)–(p) Same as (a)–(h) but at 700 m in MF. In (e), (f), (m), and (n) A refers to the mean amplitude during the case period, and σ represents one standard deviation.

the higher instantaneous amplitude ($> A + \sigma$) on 23 July relative to 22 July confirms that the warm frontal system can enhance the amplitude of IOs [Fig. S11(c)]. The marginal spectrum is computed by integrating the HS along the time axis. It represents the variation of signal energy distribution with frequency. Figs. 8(g) and (h) and S11(d) show the distribution of the marginal HS amplitude of IMF6 as a function of period (h). The amplitude is expected to peak around the IO period (23.3 $\pm$ 1 h).

Compared with the results of the HHT analysis in HF, the IO signal at MF is less pronounced. Using the U wind component at 0.7 km, the EMD technique yields an IMF6 component with a period of ~20 h on 25 and 26 March [Fig. 8(k)]. The same analysis for the composite wind [Fig. S11(e)] further supports a ~20 h period [Fig. S11(f)], corresponding to the IO component. However, the period exceeding 24 h in the EMD analysis of the V component indicates a synoptic-scale signal rather than an IO [Fig. 8(l)]. During the cold frontal passage, the instantaneous amplitude of IMF6 is above the mean A and even exceeds $A+\sigma$ during the case period [Fig. 8(m) and (n) and S11(g)]. In Figs. 8(o) and S11(h), the marginal HS exhibits an amplitude peak around the IO period (19.8 $\pm$ 1 h), whereas the corresponding analysis for V component [Fig. 8(p)] is less significant.

In this study, the BJ case on August 20, 2022, represents a typical SLLJ event. Applying the HHT technique to the wind speed time series, IMF5 reveals ~18 h period associated with IOs. However, the instantaneous amplitude of IMF5 is higher on 19 August than on 20 August [Fig. S12(b)], likely due to the influence of cold air intrusion at the upper levels on 19 August. Moreover, the same HHT analysis of the wind component is the least distinct in the BJ case. This suggests that HHT analysis is less suitable for investigating IOs during NLLJ events under strong synoptic forcing [Fig. S9(c)]. Only under weak or negligible synoptic forcing, the IOs become the primary driving mechanism of the LLJ, as the Coriolis effect dominates the boundary layer dynamics. This finding is also supported by a recent study [72].

B. Diurnal Cycle of Inertial Motions Associated With NLLJs

The CW hodographs of wind velocity are constructed at 0.1-km height intervals for all NLLJ events at the three sites. The highest frequency and most distinct CW hodographs are observed in July 2021 at HF (12 days), March 2022 at MF (14 days), and August 2022 at BJ (7 days). The evening transition in the atmospheric surface layer signifies the shift from a daytime convective boundary layer to a nocturnal stable layer around local sunset [73]. According to the evening transition hypothesis proposed by Blackadar [15], IOs are typically initiated during the evening transition period when surface friction decreases rapidly after sunset. If their AMPs decay due to intermittent turbulent mixing or variations in the pressure gradients, the maximum amplitude generally occurs close to the time of generation, typically around 00:00 UTC. Therefore, the diurnal cycle of inertial motions associated with NLLJs is examined at the three observational sites to further elucidate the impact of IOs on NLLJs development.

We selected data corresponding to frequencies within $\pm$0.5 h of the actual IO period from the instantaneous amplitude and frequency dataset using the HHT technique. Fig. 9 present the contours of the diurnal cycle of inertial motion AMPs derived from U and V wind speed components below 1 km in July 2021 at HF and March 2022 at MF. Red shading denotes stronger AMPs, with maximum AMPs (>7 m $\cdot$ s^{-1}) observed in the U [Fig. 9(a)] and V [Fig. 9(b)] components during the evening transition period (~19:00 LST) at HF. More generally, the inertial motions in the V component exhibit a distinct diurnal cycle within 0.3–0.7 km layer, which corresponds closely to the highest

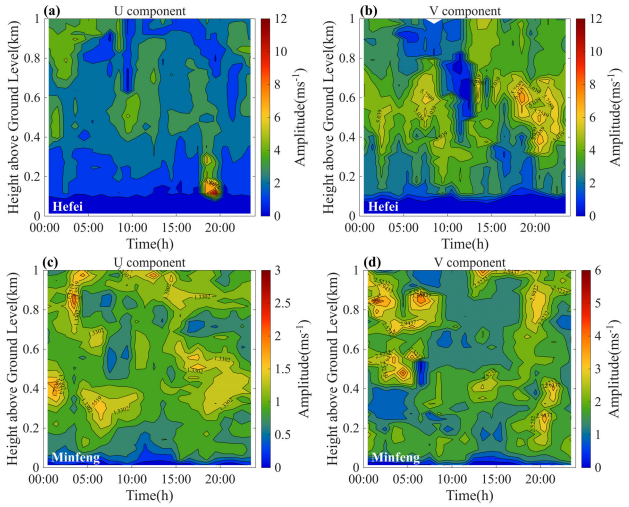

Fig. 9. Contours of the diurnal cycle of inertial motion AMPs for the U and V component as a function of height (km). (a) and (b) July 2021 at HF and (c) and (d) March 2022 in MF.

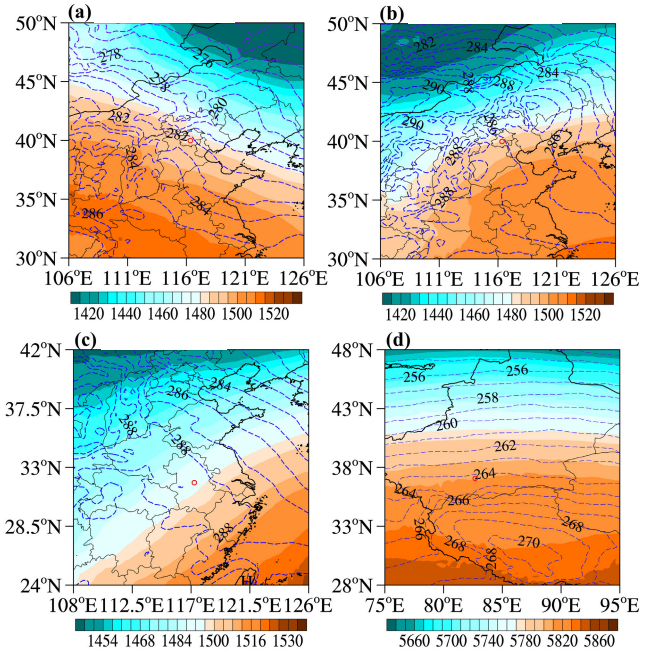

Fig. 10. Composite synoptic patterns (Type 1) associated with NLLJ events. GH fields (gpm; shaded) are shown at 850 hPa for (a) and (b) BJ, (c) HF, and (d) at 500 hPa for MF. Blue dashed contours represent atmospheric temperature fields at the corresponding pressure level. Red circles mark the locations of Doppler lidar observation sites.

occurrence height of LLJs [Fig. 4(b)]. The AMPs of inertial motions remain relatively small during the day, whereas the AMPs begin to increase after sunset (18:00 LST) and retain a large value until 07:00 LST the next morning.

Similar to HF, the diurnal cycle of inertial motion AMPs is also evident in MF. The amplitude peak (~2 m · s^{-1} in the U component occurs ~03:00 LST within 0.8–0.9 km layer [Fig. 9(c)], while the corresponding peak (~4 m · s^{-1}) in the V component appears around 01:00 LST at the same height. Within the heights of most frequent LLJs [Fig. 4(a)], large AMPs are observed in both components U (>1.7 m · s^{-1}) and V (>2.9 m · s^{-1}) between 00:00 and 06:00 LST. In particular, the AMPs of the V component begin to increase shortly after sunset and reach a local maximum (~3 m · s^{-1}) below 0.4 km. These patterns suggest that the amplitude peak bands observed at HF and MF are primarily due to the inertial motions within the atmospheric boundary layer, rather than to the diurnal cycle.

However, no amplitude peaks are observed in the U or V components during the evening transition period in August 2022 at BJ (Fig. S13). In contrast, the largest AMPs (~4 m · s^{-1}) appear around 03:00 LST below 0.5 km. Although larger AMPs (>3 m · s^{-1}) are present during the night, they do not exhibit a clear diurnal cycle within the lowest 1.5 km. The HHT analysis conducted at BJ aligns with the findings of Lundquist from the CASES-99 field experiment [69]. Accordingly, we reach a similar conclusion that the onset times and diurnal variability of inertial motions observed during NLLJ events challenge the Blackadar's evening transition hypothesis, which posits that the evening transition is the dominant mechanism for generating significant inertial motions AMPs.

C. Synoptic Forcing for NLLJ Formation

Although topographic influences and IOs are a near-daily phenomenon, LLJ events do not occur every day. The attainment of wind speeds that satisfy various LLJ criteria is fundamentally tied to forcing mechanisms associated with mid-latitude weather systems. To understand the synoptic patterns related to frequent NLLJs in three distinct locations, the geopotential height (GH) fields at 23:00 LST derived from ERA5 hourly datasets are classified by the obliquely rotated principal component analysis in the T-mode (PCA-T) method. This method applies an oblique rotation to the principal components derived from a T-mode PCA. While the standard PCA finds orthogonal (uncorrelated) components, this technique allows spatial fields of atmospheric variables over time to be correlated with each other, which can better represent the underlying structure of the data. Previous studies have demonstrated a reliable and robust performance of the PCA-T in investigating the most prominent interaction between background airflows and regional forcings such as local orography in China [74], [75].

The objective classification of the low-level GH fields and mean sea surface level (MSL) pressure associated with the NLLJs are conducted for the three sites (Figs. 10 and S14–16). In BJ, a pronounced southwest-northeast oriented pressure gradient (GSW pattern) is observed at 850 hPa, where the temperature gradient aligns with the GH gradient (Fig. 10(a); 54.7%). Another dominant synoptic pattern is featured by a southeast-northwest oriented pressure gradient (GSE pattern) at 850 hPa over BJ [Fig. 10(b); 38.8%]. The identified GSW and GSE patterns are consistent with [39], suggesting that LLJs are primarily influenced by synoptic systems associated with the Northeast China Cold Vortex (NCCV) and the Mongolian cyclone. At the surface, the dominant synoptic pattern is characterized by a south-north

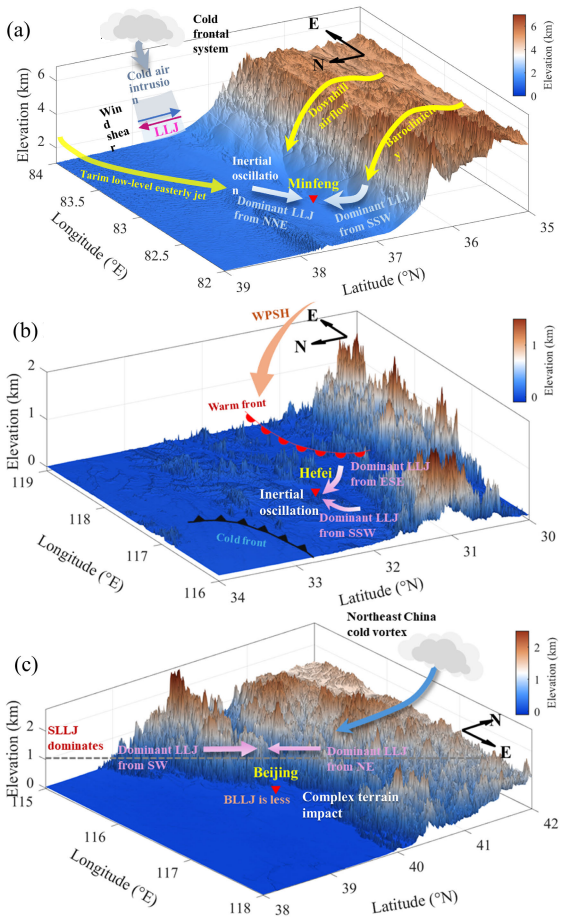

Fig. 11. Schematics illustrating the formation mechanisms of LLJs at (a) MF, (b) HF, and (c) BJ.

oriented pressure gradient and a surface anticyclone centered over the Yellow Sea with a CW circulation [Fig. S14(b)]. This configuration reinforces the thermal wind balance and enhances the vertical shear necessary for LLJs formation. The surface southwesterly winds (10-m) correspond closely with the most frequent LLJs wind direction shown in Fig. 2(f), suggesting strong surface and upper-level coupling.

In HF, the dominant synoptic pattern in MSL is characterized by a GSE pattern [Fig. S15(e); 32.1%). This pattern supports the prevailing southeasterly surface winds over HF, which aligns with the predominant LLJ wind direction in Fig. 2(e). At 850 hPa, the GH field exhibits a similar GSE pattern [Fig. 10(c); 51.0%], suggesting a coherent baroclinic structure. In contrast, the 850 hPa temperature field shows a southwest-northeast oriented gradient pattern. This misalignment between thermal and pressure gradients indicates enhanced thermal advection and vertical wind shear, which is favorable for the development and maintenance of LLJ. In MF, the GH field at 500 hPa shows a well-defined zonal flow pattern (Fig. 10(d); 63.5%), accompanied by large-scale easterly LLJ in the upper level. The dominant synoptic pattern at MSL [Fig. S16(c)] suggests that the NLLJs in MF are primarily influenced by thermal forcing induced by local topography. This is reflected in the surface pressure transition zone between Tibetan High (1024 hPa) and Tarim Low (1003 hPa) with associated southerly winds.

D. Relationship Between ML and NLLJ

In this study, we provide a brief exploration of the relationship between the evolution of the ML evolution and NLLJ (Fig. S18). On NLLJ days in MF and HF, the ML develops more rapidly from 12:00 LST and ML heights are significantly higher during the afternoon and nighttime compared to non-NLLJ days. Furthermore, ML heights of the following day also remain elevated when NLLJ occurs on the previous day. Our findings are consistent with those of [42], which suggests that the occurrence of NLLJ promotes the development of a deep ML during the day. Given the complexity of this interaction, we aim to conduct a more in-depth investigation in future research.

V. Conclusion

This study investigates the spatiotemporal characteristics of LLJs and their driving mechanisms based on one-year Doppler lidar observations at three sites in China, including MF, HF, and BJ, representing contrasting surface and environmental conditions. Clear regional differences in LLJ regimes are identified. LLJs in MF and HF are predominantly BLJs, with occurrence frequencies of 19.6% and 14.8%, respectively. In contrast, synoptic-system-related LLJs (SLLJs) are prevalent in BJ with a frequency of 21.2%. A double-nose structure of boundary layer jets is also notable at 0.5 km. In contrast, the frequency of SLLJs shows a peak at 1.4 km in HF. Among the four LLJ categories, LLJ-1 is the most frequent at all sites. The most frequent jet core heights are concentrated at 0.4 km in HF, and at 0.5 and 0.7 km in MF. In BJ, the frequency of occurrence peaks at 1.5 km and is the highest between 1 and 1.5 km layer. A consistent feature across all sites is that jet core heights increase when more stringent wind-speed criteria are applied.

The diurnal variability of LLJs exhibits pronounced nocturnal enhancement, with frequencies generally exceeding 30% from 21:00 to 06:00 LST. The maximum nocturnal frequency occurs at 22:00 LST in BJ and HF, and at 23:00 LST in MF. BJ also experiences the most prominent afternoon LLJ activity (frequency>17%) and the highest occurrence of LLJ-4. The time of lowest LLJ frequency displays a longitudinal time lag, aligning with the diurnal variation in peak height of ML. Seasonally, LLJ-1 occurrence peaks in August (24.4%) at MF, June (22.5%) at HF, May and August (28.0%) at BJ. Furthermore, LLJ-1 in BJ consistently maintains the highest frequency (>11%) year-round.

To investigate the role of IOs in NLLJ development, the ERS and HHT methods are applied to frontal case studies, including cold fronts in BJ and MF and a warm front in HF. ERS results show that the strongest IOs occur near jet core heights of 0.6 km in HF, 1.0 km in BJ, and 0.6 km in MF. The observed inertial frequency (f_a) slightly deviates from the Coriolis frequency (f_c) in HF (f_a/f_c = 1.03/1.06 cpd) and BJ

(f_a/f_c = 1.31/1.29 cpd), while good agreement is found in MF (1.21 cpd). HHT analysis further demonstrates that the IO AMPs intensify in HF and MF while the signal is the least distinct in BJ. Moreover, the temporal variation in the AMP coincides with the influence of frontal passages in HF and MF. The marginal HS reveals an amplitude peak near an inertial period of 23.3 $\pm$ 1 h in HF and 19.8 $\pm$ 1 h in MF. A clear diurnal cycle of inertial motions is observed in HF and BJ, characterized by weak daytime AMPs, rapid growth during the evening transition, and sustained enhancement overnight. Under strong synoptic forcing, as in BJ SLLJ cases, the HHT method is less effective in isolating inertial motions.

Synoptic patterns associated with NLLJs are identified using the objective classification of GH and MSL pressure fields. A dominant zonal flow pattern at 500 hPa characterizes MF, while HF is mainly influenced by southeast-northwest oriented pressure gradient (GSE) pattern at both the surface and 850 hpa. In BJ, southwest-northeast oriented pressure gradient (GSW) and GSE patterns at 850 hPa are most prominent. In MF [Fig. 11(a)], the dominant south-southwest and north-northeast jets are linked to cold fronts, easterly jets in the Tarim Basin, and terrain-induced baroclinicity associated with the Tibetan Plateau [42]. Located in the subtropical moist monsoon climate zone, both cold and warm frontal systems frequently influence HF and promote NLLJ formation [Fig. 11(b)]. Moreover, seasonal variation in HF LLJs is highly associated with the East Asian monsoon system and the Western Pacific Subtropical High [41]. In BJ, the NCCV emerges as the dominant synoptic driver, with the complex terrain (e.g., the Taihang and the Yanshan Mountains) further modulating LLJ occurrence and intensity, particularly for boundary-layer-sensitive LLJ-1 events [Fig. 11(c)].

This study provides observational evidence that NLLJs can contribute to the development of a deeper ML. While the physical processes governing LLJ formation are complex and may vary across different locations, the influence of topography on LLJ formation at the three sites is not fully resolved in this study, which represents a limitation. Future studies will benefit from longer-term observations, an expanded network of observation sites, and the integration of numerical modeling to further investigate terrain effects and regional variability of LLJs.

REFERENCES

[1] W. D. Bonner, "Climatology of the low level jet," *Monthly Weather Rev.*, vol. 96, no. 12, pp. 833–850, Dec. 1968, doi: 10.1175/1520-0493(1968)096<0833:cotllj>2.0.co;2.

[2] R. B. Stull, *An Introduction to Boundary Layer Meteorology*. Boston, MA, USA: Kluwer, 1988.

[3] R. Ranjha, G. Svensson, M. Tjernström, and A. Semedo, "Global distribution and seasonal variability of coastal low-level jets derived from ERA-interim reanalysis," *Tellus A, Dyn. Meteorol. Oceanogr.*, vol. 65, no. 1, p. 20412, Dec. 2013, doi: 10.3402/tellusa.v65i0.20412.

[4] E. Dieudonné, H. Delbarre, A. Sokolov, F. Ebojie, P. Augustin, and M. Fourmentin, "Characteristics of the low-level jets observed over dunkerque (North sea French coast) using 4 years of wind LiDAR data," *Quart. J. Roy. Meteorological Soc.*, vol. 149, no. 754, pp. 1745–1768, Jul. 2023, doi: 10.1002/qj.4480.

[5] F. M. Ralph, P. J. Neiman, and R. Rotunno, "Dropsonde observations in low-level jets over the northeastern Pacific Ocean from CALJET-1998 and PACJET-2001: Mean vertical-profile and atmospheric-river characteristics," *Monthly Weather Rev.*, vol. 133, no. 4, pp. 889–910, Apr. 2005, doi: 10.1175/mwr2896.1.

[6] M. P. Sánchez et al., "Observational investigation of the low-level jets in the metropolitan region of São Paulo, Brazil," *Earth Space Sci.*, vol. 9, no. 9, p. 2021, Sep. 2022, doi: 10.1029/2021ea002190.

[7] J. Cuxart and M. A. Jiménez, "Mixing processes in a nocturnal low-level jet: An LES study," *J. Atmos. Sci.*, vol. 64, no. 5, pp. 1666–1679, May 2007, doi: 10.1175/jas3903.1.

[8] A. Gevorgyan, "A case study of low-level jets in yerevan simulated by the WRF model," *J. Geophys. Res., Atmos.*, vol. 123, no. 1, pp. 300–314, Jan. 2018, doi: 10.1002/2017jd027629.

[9] M.-Y. He, H.-B. Liu, B. Wang, and D.-L. Zhang, "A modeling study of a low-level jet along the yun-gui Plateau in South China," *J. Appl. Meteorol. Climatol.*, vol. 55, no. 1, pp. 41–60, Jan. 2016, doi: 10.1175/jamc-d-15-0067.1.

[10] G. Jiménez-Sánchez, P. M. Markowski, V. Jewtoukoff, G. S. Young, and D. J. Stensrud, "The orinoco low-level jet: An investigation of its characteristics and evolution using the WRF model," *J. Geophys. Res., Atmos.*, vol. 124, no. 20, pp. 10696–10711, Oct. 2019, doi: 10.1029/2019jd030934.

[11] J. A. Aird, R. J. Barthelmie, T. J. Shepherd, and S. C. Pryor, "Occurrence of low-level jets over the eastern U.S. coastal zone at heights relevant to wind energy," *Energies*, vol. 15, no. 2, p. 445, Jan. 2022, doi: 10.3390/en15020445.

[12] W. Wei, H. Zhang, X. Zhang, and H. Che, "Low-level jets and their implications on air pollution: A review," *Frontiers Environ. Sci.*, vol. 10, 2023, Art. no. 1082623, doi: 10.3389/fenvs.2022.1082623.

[13] B. Wu, Z. Li, T. Ju, and H. Zhang, "Characteristics of low-level jets during 2015–2016 and the effect on fog in Tianjin," *Atmos. Res.*, vol. 245, Nov. 2020, Art. no. 105102, doi: 10.1016/j.atmosres.2020.105102.

[14] Y. Du and R. Rotunno, "A simple analytical model of the nocturnal low-level jet over the great plains of the United States," *J. Atmos. Sci.*, vol. 71, no. 10, pp. 3674–3683, Oct. 2014, doi: 10.1175/jas-d-14-0060.1.

[15] A. K. Blackadar, "Boundary layer wind maxima and their significance for the growth of nocturnal inversions," *Bull. Amer. Meteorological Soc.*, vol. 38, no. 5, pp. 283–290, May 1957, doi: 10.1175/1520-0477-38.5.283.

[16] W. D. Bonner and J. Paegle, "Diurnal variations in boundary layer winds over the south-central United States in summer," *Monthly Weather Rev.*, vol. 98, no. 10, pp. 735–744, Oct. 1970.

[17] B. J. H. Van de Wiel, A. F. Moene, G. J. Steeneveld, P. Baas, F. C. Bosveld, and A. A. M. Holtslag, "A conceptual view on inertial oscillations and nocturnal low-level jets," *J. Atmos. Sci.*, vol. 67, no. 8, pp. 2679–2689, Aug. 2010, doi: 10.1175/2010jas3289.1.

[18] J. Kutsher, N. Haikin, A. Sharon, and E. Heifetz, "On the formation of an elevated nocturnal inversion layer in the presence of a low-level jet: A case study," *Boundary-Layer Meteorol.*, vol. 144, no. 3, pp. 441–449, Sep. 2012, doi: 10.1007/s10546-012-9720-y.

[19] J. R. Holton, "The diurnal boundary layer wind oscillation above sloping terrain[1]," *Tellus A, Dyn. Meteorol. Oceanogr.*, vol. 19, no. 2, p. 199, Jan. 1967, doi: 10.3402/tellusa.v19i2.9766.

[20] H. Wexler, "A boundary layer interpretation of the low-level jet," *Tellus*, vol. 13, no. 3, pp. 368–378, Aug. 1961, doi: 10.1111/j.2153-3490.1961.tb00098.x.

[21] C. Saulo, J. Ruiz, and Y. G. Skabar, "Synergism between the low-level jet and organized convection at its exit region," *Monthly Weather Rev.*, vol. 135, no. 4, pp. 1310–1326, Apr. 2007, doi: 10.1175/mwr3317.1.

[22] L. W. Uccellini, R. A. Petersen, P. J. Kocin, K. F. Brill, and J. J. Tuccillo, "Synergistic interactions between an upper-level jet streak and diabatic processes that influence the development of a low-level jet and a secondary coastal cyclone," *Monthly Weather Rev.*, vol. 115, no. 10, pp. 2227–2261, Oct. 1987.

[23] Y. Du, Y.-L. Chen, and Q. Zhang, "Numerical simulations of the boundary layer jet off the Southeastern coast of China," *Monthly Weather Rev.*, vol. 143, no. 4, pp. 1212–1231, Apr. 2015, doi: 10.1175/mwr-d-14-00348.1.

[24] T. R. Holt, "Mesoscale forcing of a boundary layer jet along the California coast," *J. Geophys. Res., Atmos.*, vol. 101, no. D2, pp. 4235–4254, Feb. 1996, doi: 10.1029/95jd03231.

[25] W. Wei, H. S. Zhang, and X. X. Ye, "Comparison of low-level jets along the north coast of China in summer," *J. Geophys. Research: Atmos.*, vol. 119, no. 16, pp. 9692–9706, Aug. 2014, doi: 10.1002/2014jd021476.

[26] Y. Du and G. Chen, "Heavy rainfall associated with double low-level jets over southern China. Part II: Convection initiation," *Monthly Weather Rev.*, vol. 147, no. 2, pp. 543–565, Feb. 2019, doi: 10.1175/mwr-d-18-0102.1.

[27] Y. Du and G. Chen, "Climatology of low-level jets and their impact on rainfall over southern China during the early-summer rainy season," *J. Climate*, vol. 32, no. 24, pp. 8813–8833, Dec. 2019, doi: 10.1175/jcli-d-19-0306.1.

[28] X. Huang, C. Zhang, J. Fei, X. Cheng, J. Ding, and H. Liu, "Uplift mechanism of coastal extremely persistent heavy rainfall (EPHR): The key role of low-level jets and ageostrophic winds in the boundary layer," *Geophys. Res. Lett.*, vol. 49, no. 8, p. 2021, Apr. 2022, doi: 10.1029/2021gl096029.

[29] N. Li et al., "Low-level jet and its effect on the onset of summertime nocturnal rainfall in Beijing," *Geophys. Res. Lett.*, vol. 51, no. 20, p. 2024, Oct. 2024, doi: 10.1029/2024gl110840.

[30] X. Li and Y. Du, "Statistical relationships between two types of heavy rainfall and low-level jets in South China," *J. Climate*, vol. 34, no. 21, pp. 8549–8566, Nov. 2021, doi: 10.1175/jcli-d-21-0121.1.

[31] L. Su, J. Hu, Y. Du, J. Li, and G. Chen, "Boundary-layer and low-level moisture fluxes during low-level jet events in South China and their relationship with early summer rainfall," *J. Climate*, vol. 38, no. 7, pp. 1691–1713, Apr. 2025, doi: 10.1175/jcli-d-23-0561.1.

[32] F. Dong, X. Zhi, L. Zhang, and C. Ye, "Diurnal variations of coastal boundary layer jets over the northern South China sea and their impacts on diurnal cycle of rainfall over southern China during the early-summer rainy season," *Monthly Weather Rev.*, vol. 149, no. 10, pp. 3341–3363, Oct. 2021, doi: 10.1175/mwr-d-20-0292.1.

[33] H. Kong, Q. Zhang, Y. Du, and F. Zhang, "Characteristics of coastal low-level jets over Beibu Gulf, China, during the early warm season," *J. Geophys. Res., Atmos.*, vol. 125, no. 14, 2020, Art. no. e2019JD031918, doi: 10.1029/2019jd031918.

[34] X. Liu, Y. Luo, L. Huang, D.-L. Zhang, and Z. Guan, "Roles of double low-level jets in the generation of coexisting inland and coastal heavy rainfall over South China during the presummer rainy season," *J. Geophys. Res., Atmos.*, vol. 125, no. 18, p. 2020, Sep. 2020, doi: 10.1029/2020jd032890.

[35] Y. Du, Q. Zhang, Y.-L. Chen, Y. Zhao, and X. Wang, "Numerical simulations of spatial distributions and diurnal variations of low-level jets in China during early summer," *J. Climate*, vol. 27, no. 15, pp. 5747–5767, Aug. 2014, doi: 10.1175/jcli-d-13-00571.1.

[36] Y. Yan, X. Cai, X. Wang, Y. Miao, and Y. Song, "Low-level jet climatology of China derived from long-term radiosonde observations," *J. Geophys. Res., Atmos.*, vol. 126, no. 20, p. 2021, Oct. 2021, doi: 10.1029/2021jd035323.

[37] J. M. Ge, H. Liu, J. Huang, and Q. Fu, "Taklimakan desert nocturnal low-level jet: Climatology and dust activity," *Atmos. Chem. Phys.*, vol. 16, no. 12, pp. 7773–7783, Jun. 2016, doi: 10.5194/acp-16-7773-2016.

[38] D. Li et al., "Low-level jets over the Bohai Sea and Yellow Sea: Climatology, variability, and the relationship with regional atmospheric circulations," *J. Geophys. Res., Atmos.*, vol. 123, no. 10, pp. 5240–5260, May 2018, doi: 10.1029/2017jd027949.

[39] Y. Miao et al., "The climatology of low-level jet in Beijing and Guangzhou, China," *J. Geophys. Res., Atmos.*, vol. 123, no. 5, pp. 2816–2830, Mar. 2018, doi: 10.1002/2017jd027321.

[40] L. Zhou, C. Wang, S. Miao, and J. Li, "Impact of the complex terrain in Beijing on formation of low-level jets," *J. Meteorological Res.*, vol. 38, no. 1, pp. 138–150, Feb. 2024, doi: 10.1007/s13351-024-3122-1.

[41] T. Wei, M. Wang, K. Wu, J. Yuan, H. Xia, and S. Lolli, "Characterizing urban planetary boundary layer dynamics using 3-year Doppler wind LiDAR measurements in a western Yangtze river delta city, China," *Atmos. Meas. Techn.*, vol. 18, no. 8, pp. 1841–1857, Apr. 2025, doi: 10.5194/amt-18-1841-2025.

[42] L. Su, C. Lu, J. Yuan, X. Wang, Q. He, and H. Xia, "Measurement report: The promotion of the low-level jet and thermal effects on the development of the deep convective boundary layer at the Southern edge of the Taklimakan desert," *Atmos. Chem. Phys.*, vol. 24, no. 18, pp. 10947–10963, Sep. 2024, doi: 10.5194/acp-24-10947-2024.

[43] S. Kameyama, T. Ando, K. Asaka, Y. Hirano, and S. Wadaka, "Compact all-fiber pulsed coherent Doppler LiDAR system for wind sensing," *Appl. Opt.*, vol. 46, no. 11, pp. 1953–1962, Apr. 2007, doi: 10.1364/ao.46.001953.

[44] F. Späth et al., "Simultaneous observations of surface layer profiles of humidity, temperature, and wind using scanning LiDAR instruments," *J. Geophys. Res., Atmos.*, vol. 127, no. 5, p. 2021, Mar. 2022, doi: 10.1029/2021jd035697.

[45] D. Yu, Q. Zhang, Y. Ying, and Y. Yang, "Characteristics of low-level jets in Shanghai during the 2008–2009 warm seasons as inferred from wind profiler radar data," *J. Meteorological Soc. Jpn. II*, vol. 90, no. 6, pp. 891–903, 2012, doi: 10.2151/jmsj.2012-603.

[46] B. J. Carroll, B. B. Demoz, and R. Delgado, "An overview of low-level jet winds and corresponding mixed layer depths during PECAN," *J. Geophys. Res., Atmos.*, vol. 124, no. 16, pp. 9141–9160, Aug. 2019, doi: 10.1029/2019jd030658.

[47] Y. L. Pichugina et al., "Doppler LiDAR measurements of wind variability and LLJ properties in central Oklahoma during the August 2017 land–atmosphere feedback experiment," *J. Appl. Meteorol. Climatol.*, vol. 62, no. 8, pp. 947–969, Aug. 2023, doi: 10.1175/jamc-d-22-0128.1.

[48] M. Friedl, J. Gray, and D. Sulla-Menashe, "MODIS/terra+aqua land cover dynamics yearly L3 global 500m SIN grid V061," NASA EOSDIS Land Processes Distrib. Act. Arch. Center (DAAC), Sioux Falls, SD, USA, Tech. Rep. MCD12Q2-061, 2022, doi: 10.5067/MODIS/MCD12Q2.061.

[49] N. Nasierding and Y. Zhang, "Change detection of sandy land areas in minfeng oasis of xinjiang, China," *Environ. Monit. Assess.*, vol. 151, nos. 1–4, pp. 189–196, Apr. 2008, doi: 10.1007/s10661-008-0260-3.

[50] T. Wei et al., "Simultaneous wind and rainfall detection by power spectrum analysis using a VAD scanning coherent Doppler LiDAR," *Opt. Exp.*, vol. 27, no. 22, pp. 31235–31245, Oct. 2019, doi: 10.1364/oe.27.031235.

[51] T. Wei, H. Xia, B. Yue, Y. Wu, and Q. Liu, "Remote sensing of raindrop size distribution using the coherent Doppler LiDAR," *Opt. Exp.*, vol. 29, no. 11, pp. 17246–17257, May 2021, doi: 10.1364/oe.426326.

[52] T. Wei et al., "Retrieving aerosol backscatter coefficient using coherent Doppler wind LiDAR," *Opt. Exp.*, vol. 33, no. 4, p. 6832, Feb. 2025, doi: 10.1364/oe.551730.

[53] L. Su, H. Xia, J. Yuan, Y. Wang, A. Maituerdi, and Q. He, "Study on daytime atmospheric mixing layer height based on 2-year coherent Doppler wind LiDAR observations at the southern edge of the Taklimakan desert," *Remote Sens.*, vol. 16, no. 16, p. 3005, Aug. 2024, doi: 10.3390/rs16163005.

[54] I. Algarra, J. Eiras-Barca, R. Nieto, and L. Gimeno, "Global climatology of nocturnal low-level jets and associated moisture sources and sinks," *Atmos. Res.*, vol. 229, pp. 39–59, Nov. 2019, doi: 10.1016/j.atmosres.2019.06.016.

[55] D. C. A. Lima, P. M. M. Soares, M. Nogueira, and A. Semedo, "Global coastal low-level wind jets revisited through the new ERA5 reanalysis," *Int. J. Climatol.*, vol. 42, no. 9, pp. 4491–4507, Jul. 2022, doi: 10.1002/joc.7482.

[56] E. W. Luiz and S. Fiedler, "Global climatology of low-level-jets: Occurrence, characteristics, and meteorological drivers," *J. Geophys. Res., Atmos.*, vol. 129, no. 9, p. 2023, May 2024, doi: 10.1029/2023jd040262.

[57] T. Wei, H. Xia, Y. Wu, J. Yuan, C. Wang, and X. Dou, "Inversion probability enhancement of all-fiber CDWL by noise modeling and robust fitting," *Opt. Exp.*, vol. 28, no. 20, pp. 29662–29675, Sep. 2020, doi: 10.1364/oe.401054.

[58] E. J. O'Connor et al., "A method for estimating the turbulent kinetic energy dissipation rate from a vertically pointing Doppler LiDAR, and independent evaluation from balloon-borne in situ measurements," *J. Atmos. Ocean. Technol.*, vol. 27, no. 10, pp. 1652–1664, Oct. 2010, doi: 10.1175/2010jtecha1455.1.

[59] V. A. Banakh, I. N. Smalikho, and A. V. Falits, "Estimation of the turbulence energy dissipation rate in the atmospheric boundary layer from measurements of the radial wind velocity by micropulse coherent Doppler LiDAR," *Opt. Exp.*, vol. 25, no. 19, p. 22679, Sep. 2017, doi: 10.1364/oe.25.022679.

[60] M. P. A. da Silva, F. Rocadenbosch, R. L. Tanamachi, and U. Saeed, "Motivating a synergistic mixing-layer height retrieval method using backscatter LiDAR returns and microwave-radiometer temperature observations," *IEEE Trans. Geosci. Remote Sens.*, vol. 60, 2022, Art. no. 4107418, doi: 10.1109/TGRS.2022.3158401.

[61] V. A. Banakh, I. N. Smalikho, and A. V. Falits, "Estimation of the height of the turbulent mixing layer from data of Doppler LiDAR measurements using conical scanning by a probe beam," *Atmos. Meas. Techn.*, vol. 14, no. 2, pp. 1511–1524, Feb. 2021, doi: 10.5194/amt-14-1511-2021.

[62] L. Wang, J. Yuan, H. Xia, L. Zhao, and Y. Wu, "Marine mixed layer height detection using ship-borne coherent Doppler wind LiDAR based on constant turbulence threshold," *Remote Sens.*, vol. 14, no. 3, p. 745, Feb. 2022, doi: 10.3390/rs14030745.

[63] C. D. Whiteman, X. Bian, and S. Zhong, "Low-level jet climatology from enhanced rawinsonde observations at a site in the southern great plains," *J. Appl. Meteorol.*, vol. 36, no. 10, pp. 1363–1376, Oct. 1997, doi: 10.1175/1520-0450(1997)036<1363:lljcfe>2.0.co;2.

[64] N. E. Huang et al., "The empirical mode decomposition and the Hilbert spectrum for nonlinear and non-stationary time series analysis," *Proc. Roy. Soc. London. A, Math., Phys. Eng. Sci.*, vol. 454, no. 1971, pp. 903–995, Mar. 1998, doi: 10.1098/rspa.1998.0193.

[65] N. E. Huang and S. S. P. Shen, "Hilbert–Huang transform and its applications," in *Interdisciplinary Mathematical Sciences*, vol. 5. Singapore: World Scientific, 2005.

[66] J. Barat and C. Cot, "Wind shear rotary spectra in the atmosphere," *Geophys. Res. Lett.*, vol. 19, no. 2, pp. 103–106, Jan. 1992, doi: 10.1029/92gl00044.

[67] A. de la Torre et al., "A spectral rotary analysis of gravity waves: An application during one of the SOUTHTRAC flights," *J. Geophys. Res., Atmos.*, vol. 128, no. 1, p. 2022, Jan. 2023, doi: 10.1029/2022jd037139.

[68] D. C.-F. Shih, "Rotary spectral analysis for directional time series: Seasonal variation of wind speed on a subtropical island near the western Pacific Ocean," *Pure Appl. Geophysics*, vol. 178, no. 4, pp. 1369–1385, Apr. 2021, doi: 10.1007/s00024-021-02708-z.

[69] J. K. Lundquist, "Intermittent and elliptical inertial oscillations in the atmospheric boundary layer," *J. Atmos. Sci.*, vol. 60, no. 21, pp. 2661–2673, Nov. 2003, doi: 10.1175/1520-0469(2003)060<2661:iaeioi>2.0.co;2.

[70] Y. Mori, "Evidence of inertial oscillations of the surface wind at Marcus Island," *J. Geophys. Res., Atmos.*, vol. 95, no. D8, pp. 11777–11783, Jul. 1990, doi: 10.1029/jd095id08p11777.

[71] W. Wei, B. G. Wu, X. X. Ye, H. X. Wang, and H. S. Zhang, "Characteristics and mechanisms of low-level jets in the Yangtze river delta of China," *Boundary-Layer Meteorol.*, vol. 149, no. 3, pp. 403–424, Dec. 2013, doi: 10.1007/s10546-013-9852-8.

[72] F. Barbano, L. S. Leo, L. Brogno, and S. Di Sabatino, "Inertial oscillation modelling of low-level jets: An application to the complex terrain and double-nosed wind profiles," *Bull. Atmos. Sci. Technol.*, vol. 5, no. 1, p. 7, Jul. 2024, doi: 10.1007/s42865-024-00070-1.

[73] R. Cheng, E. Pardyjak, and C. Hang, "Evening transition thermal processes and flow dynamics over opposing slopes of an isolated mountain," *Quart. J. Roy. Meteorological Soc.*, p. 70051, Nov. 2025, Art. no. e70051, doi: 10.1002/qj.70051.

[74] L. Bai, G. Chen, Y. Huang, and Z. Meng, "Convection initiation at a coastal rainfall hotspot in South China: Synoptic patterns and orographic effects," *J. Geophys. Res., Atmos.*, vol. 126, no. 24, p. 2021, Dec. 2021, doi: 10.1029/2021jd034642.

[75] C. Wang, K. Zhao, A. Huang, X. Chen, and X. Rao, "The crucial role of synoptic pattern in determining the spatial distribution and diurnal cycle of heavy rainfall over the South China coast," *J. Climate*, vol. 34, no. 7, pp. 2441–2458, Apr. 2021, doi: 10.1175/jcli-d-20-0274.1.